



ARTICLE

A Mathematical Model and Simulations of Low Temperature Nitriding

Katarzyna Tkacz-Śmiech Deceased. We dedicate this article to the memory of Professor Katarzyna Tkacz-Śmiech

Bogusław Bożek¹, Lucjan Sapa^{1,*}, Katarzyna Tkacz-Śmiech², Marek Danielewski² and Janusz Rybak²

¹AGH University of Science and Technology, Faculty of Applied Mathematics, Cracow, 30-059, Poland

²AGH University of Science and Technology, Faculty of Materials Science and Ceramics, Cracow, 30-059, Poland

*Corresponding Author: Lucjan Sapa. Email: sapa@agh.edu.pl

Received: 02 June 2021 Accepted: 10 September 2021

ABSTRACT

Low-temperature nitriding of steel or iron can produce an expanded austenite phase, which is a solid solution of a large amount of nitrogen dissolved interstitially in fcc lattice. It is characteristic that the nitrogen depth profiles in expanded austenite exhibit plateau-type shapes. Such behavior cannot be considered with a standard analytic solution for diffusion in a semi-infinite solid and a new approach is necessary. We formulate a model of interdiffusion in viscoelastic solid (Maxwell model) during the nitriding process. It combines the mass conservation and Vegard's rule with the Darken *bi*-velocity method. The model is formulated in any dimension, i.e., a mixture is included in \mathbb{R}^n , $n = 1, 2, 3$. For the system in one dimension, $n = 1$, we transform a differential-algebraic system of 5 equations to a differential system of 2 equations only, which is better to study numerically and analytically. Such modification allows the formulation of effective mixed-type boundary conditions. The resulting nonlinear strongly coupled parabolic-elliptic differential initial-boundary Stefan type problem is solved numerically and a series of simulations is made.

KEYWORDS

Nitriding; expanded austenite; Maxwell solid; Darken method; Vegard rule

List of symbols

1, 2	Components, 1 \equiv Fe, 2 \equiv N
Ω_i	Partial molar volume of the <i>i</i> -th component
Ω	Molar volume of the mixture
D_i	Diffusivity of the <i>i</i> -th component
B_i	Mobility of the <i>i</i> -th component
T	Temperature
t	Time
R	Gas constant
$c_i(t, x)$	Concentration of the <i>i</i> -th component
$N_i(t, x)$	Molar ratio of the <i>i</i> -th component
$N_L^s(t)$	Surface nitrogen concentration at the left boundary
$N_{L,\infty}^s$	Steady-state nitrogen concentration at the left boundary



$y_i(t, x)$	Volume concentration of the i -th component
$c(t, x)$	Overall concentration of the mixture
$\mu_i(t, x)$	Chemical potential of the i -th component
μ_i°	Chemical potential of a reference state of the i -th component
$a_i(t, x)$	Activity of the i -th component
$f_i(t, x)$	Activity coefficient of the i -th component
$\theta_i(t, x)$	Thermodynamic factor of the i -th component
$J_i(t, x)$	Overall flux of the i -th component
$J_i^d(t, x)$	Diffusional flux of the i -th component
$P(t, x)$	Local pressure (stress)
$v(t, x)$	Local material velocity (drift velocity) velocity
η	Viscosity coefficient, $\eta^* = \frac{4}{3}\eta$
E	The Young modulus
ν_P	The Poisson number
u_0	The lattice parameter
$u(N_2)$	A linear dependence between the lattice parameter and nitrogen content in Fe
$[\Lambda_1(t), \Lambda_2]$	Domain in \mathbb{R}

Initial and boundary conditions

$Y(x)$	Initial condition for the Fe volume concentration
$P_L(t)$	Dirichlet boundary condition for the dynamic pressure at $x = \Lambda_1(t)$
$Y_L(t)$	Dirichlet boundary condition for the Fe volume concentration at $x = \Lambda_1(t)$
β	Constant parameter in $N_2^s(t)$ function
$\varphi(t)$	Time dependent function used to express $Y_L(t)$
k_f, k_b, F	Constants used in the Chang-Jaffé boundary condition for nitrogen concentration at $\Lambda_1(t)$

1 Introduction

Nitriding is a thermochemical surface treatment carried out below eutectoid temperature. In the method, a surface of a solid substrate is modified by inserting (diffusion) of nitrogen from the gas atmosphere, which leads to the development of a compound layer and diffusion zone near the substrate surface [1–3]. Nitriding has shown the potential to enhance mechanical properties of the surface layer. The compound layer can improve wear and corrosion resistance [4]. The diffusion zone, which grows beneath the compound layer, is responsible for the enhancement of fatigue strength.

Depending on a medium providing nitrogen, the nitriding process can be pack, salt-bath, gas, or plasma nitriding. In the pack nitriding, nitrogen-containing organic compounds are used as a nitrogen source. Salt-bath nitriding is carried out in a molten salt bath. In the gas nitriding process, nitrogen is supplied from the gas atmosphere, usually ammonia, NH_3 . Plasma-discharge technology is a basis for plasma nitriding [5–9]. Basically, it is a glow discharge process in a mixture of nitrogen and hydrogen gases. A bias voltage applied to the substrate causes ions to collide with the surface and enhancing the nitriding effect. Plasma nitriding is the most versatile nitriding process and has many advantages over conventional salt-bath and gas nitriding [10–15].

For the last 30 years, it has been reported in many papers that it is possible to nitride stainless steel in such way that a phase of so called expanded austenite is formed, in which nitrogen concentration can reach 38% but remains in solid solution [13,15–30]. Expanded austenite, also known as S phase or γ_N phase, is a metastable supersaturated solid solution of nitrogen (or carbon) in austenite that forms as a case by diffusion [31,32]. It provides high hardness and high resistance against wear, corrosion and fatigue, which is a consequence of compressive residual

stresses. Such stresses appear due to lattice expansion while the core material constraints the expansion. The composition-induced expansion accommodates elasto-plastically [33–35]. It has been also demonstrated that when nitriding is carried out with the use of high-intensity nitrogen plasma pulses the expanded austenite phase can be formed in ARMCO α -iron. The pure iron, initially in α phase, can be transformed into the γ austenite structure, in which expanded austenite is present [36,37]. Typical N -depth profiles in expanded austenite show high value at the surface, an abrupt decrease following a nearly constant plateau and final decrease to a matrix value. Such behavior clearly deviates from the Fickian diffusion and several models have been proposed to predict formation of the expanded austenite. Williamson et al. [38] theorized that if the Cr atoms are present in the alloy they tend to trap N atoms nearby octahedral sites. When all the Cr traps are occupied, additional N atoms rapidly diffuse to the edge of the γ_N layer. This model has been mathematically formalized by Parascandola et al. [39] basing on the diffusion equation with trapping and detrapping and has been accepted by many authors [19,20,31,32]. In several papers [18,21,22], the non-Fickian distribution of nitrogen has been modeled by assuming a presence of composition-dependent internal stress gradient generated by the nitrogen penetration. The stress gradient yields an additional driving force for the diffusion, next to the concentration gradient.

Galdikas et al. [40] considered a simple case, namely the diffusion flux of nitrogen J_N being proportional to the gradient of chemical potential $\mu_N(c_N, T, p)$, depending on the nitrogen concentration c_N , temperature T , and pressure p . Moreover they examined a degenerated situation when the pressure p in solids is proportional to internal stresses: $p = -\sigma$. In simple words the pressure is the hydrostatic part of the stress tensor, is analogue of the hydrostatic pressure. They neglected the interdiffusion in Fe-N system, consequently a drift was not analyzed and ignore plastic deformation (in our work we consider the Maxwell solid). They had also different, mathematically complicated boundary conditions on the nitrogen concentration c_N given by a suitable differential equation. Kücüküydiz et al. [41] modeled the low temperature plasma nitriding, $T \in [420^\circ\text{C}, 445^\circ\text{C}]$, of austenitic stainless steels, i.e., the reactive diffusion of nitrogen in isotropic elasto-plastic material. At such temperature the diffusivities of metals are very low and interdiffusion process is negligible. The one-dimensional model combines the diffusion of nitrogen, $D_N(c_N, T)$, the elasto-plastic accommodation of the lattice expansion, the solid solution-strengthening by nitrogen and the reactions (trapping of nitrogen by chromium atoms). A very good agreement was found between the predicted and experimental composition-depth profiles.

A treatment, which takes into account internal stresses, stress relaxation and the resulting convective transport has been developed by Stephenson [42,43]. In his works, Stephenson focuses on the solution in an arbitrary binary system but a discussion of binary conditions is lacking. In this research, we use a similar approach as it has been presented by Stephenson in [42,43] and in our earlier paper [44]. Namely, we combine the Darken bi-velocity method with the Vegard rule, the Maxwell model of viscoelastic material and the Gibbs-Duhem equation on chemical potentials. We formulate the model in any dimension. In one dimensional case, we equivalently transform such a differential-algebraic system of 5 equations to a differential system of 2 equations only. This modification allows us giving effective mixed type boundary conditions. The open boundary changes with time. Such a nonlinear strongly coupled parabolic-elliptic differential initial-boundary Stefan type problem is solved numerically using the constructed implicit finite difference methods. They are generated by some linearization and splitting ideas. From a numerical and analytical point of view, it is better to study the reduced differential system of 2 equations than the differential-algebraic system of 5 equations proposed by Stephenson. The interdiffusion during the nitriding

is simulated in one dimension and different boundary conditions are discussed. A comparison of our numerical simulations with simulations obtained with the use of some known physically simpler models, for example given in [40], we will present in our future papers.

2 Theory

The overall interdiffusion process can involve a variety of interactions between the diffusive transport, internal stresses, convection (drift) and deformation (plastic strain). Fundamental studies of Larche et al. [45] concerning the stress generated during the interdiffusion and its contribution to a diffusion potential neglect stress relaxation and convective transport due to the plastic deformation. In the Darken method, the potential necessary to drive the plastic deformation is neglected and it is assumed that plastic flow occurs sufficiently rapidly. In such case, the diffusion of a “faster” component is rate-limiting. At relatively small distances, like in the surface layer, the diffusion of “slower” component can become the rate limiting step. When it is true, a simple diffusion equation is not sufficient to describe the overall interdiffusion. A treatment which takes into account both internal stresses, stress relaxation and the resulting convective transport has been developed by Stephenson [42,43]. In the present study, we extend this idea and consider interdiffusion vector fluxes $J_i = J_i(t, x) \in \mathbb{R}^n$, $x \in \Sigma = \Sigma(t) \subset \mathbb{R}^n$, $n = 1, 2, 3$, $i = 1, \dots, s$ in the s component system given constitutive equations:

$$J_i = -B_i c_i (\nabla \mu_i + \Omega_i \nabla P) + c_i v, \quad i = 1, \dots, s, \quad (1)$$

where B_i , Ω_i , $c_i = c_i(t, x)$, $\mu_i = \mu_i(t, x)$ are mobility, partial molar volume, concentration of the i th specie and its chemical potential. It is assumed that B_i and Ω_i are constant, i.e., composition independent. $P = P(t, x)$ is the local pressure and $v = v(t, x)$ is the local material velocity (drift) common for all components [46–48].

The first term in (1) describes chemical diffusion due to the gradient of the chemical potential. The second and third terms represent diffusion due to the non-uniform stress and convective transport, respectively. Convection generates viscous flow and the use of proper constitutive relation is mandatory at low temperatures. A good choice is the Maxwell solid.

Viscoelasticity is a property of materials that exhibits both viscous and elastic characteristics when undergoing deformation. The Maxwell model predicts that when a material is put under stress, the strain has two components: (i) an elastic component occurring instantaneously and corresponding to the spring, which relaxes immediately upon release of the stress; (ii) viscous component that decreases with time as long as the stress is applied which seems accurate for interdiffusion at short distances.

Let us use a simple example of the two-component interdiffusion, $s = 2$, for example between the solid metallic substrate (Me) and nitrogen (N) from a gas atmosphere. It is assumed that partial molar volumes and the diffusivities of the Me , N components are constant, i.e., concentration independent. Consider the following physical equations.

Continuity equations:

$$\frac{\partial c_i}{\partial t} = -\nabla \cdot J_i, \quad i = 1, 2, \quad 1 \equiv Me, \quad 2 \equiv N. \quad (2)$$

The overall flux J_i of the specie in (2) is given by (1). The symbol “ \cdot ” stands for the standard inner product in \mathbb{R}^n .

Vegard rule:

$$\Omega_1 c_1 + \Omega_2 c_2 = 1. \quad (3)$$

Maxwell solid:

$$\nabla \cdot v = \frac{1}{\eta^*} P, \quad (4)$$

where $\eta^* = \frac{4}{3}\eta$ and η is the viscosity coefficient. The Maxwell solid equation determines kinetics of the plastic strain (viscous flow) and combines the convection velocity v with the pressure P .

The nonideal solute chemical potential is assumed

$$\mu_i = \mu_i^\circ + RT \ln a_i = \mu_i^\circ + RT \ln (f_i N_i), \quad i = 1, 2, \quad (5)$$

where μ_i° , $a_i = a_i(N_i)$, $f_i = f_i(N_i)$ denote the chemical potential of a reference state, the component activity and the activity coefficient, and $N_i = N_i(t, x)$ is a molar ratio of the component, $N_i = \frac{c_i}{c}$, $c = c_1 + \dots + c_s$, R is the gas constant and T means the temperature. The activity coefficient will be taken a function of hydrostatic pressure, see [Part 3.1](#). Assume that f_2 can be expressed by the suitable explicit formula as a function of N_2 (see (29)) but there is not known an explicit formula on f_1 . We treat μ_2 as a known function expressed by N_2 (or equivalently c_1 , c_2) and μ_1 as an unknown.

We postulate local-equilibrium, isothermal, isobaric conditions which imply

Gibbs-Duhem equation:

$$c_1 \nabla \mu_1 + c_2 \nabla \mu_2 = 0, \quad (6)$$

or equivalently

$$N_1 \nabla \mu_1 + N_2 \nabla \mu_2 = 0. \quad (7)$$

It is easy to verify that from (2) and (3) we get

Volume continuity equation:

$$\nabla \cdot (\Omega_1 J_1 + \Omega_2 J_2) = 0. \quad (8)$$

Our object to study is the differential-algebraic system (2)–(4), (6) of 5 equations with $(4 + n)$ unknowns: c_1 , c_2 , v , P and μ_1 . It is because of $v \in \mathbb{R}^n$. Using (1) and (8) this system can be equivalently written in the following form:

$$\begin{cases} \frac{\partial c_1}{\partial t} = -\nabla \cdot (-B_1 c_1 (\nabla \mu_1 + \Omega_1 \nabla P) + c_1 v), \\ \nabla \cdot (\Omega_1 B_1 c_1 (\nabla \mu_1 + \Omega_1 \nabla P) + \Omega_2 B_2 c_2 (\nabla \mu_2 + \Omega_2 \nabla P) - v) = 0, \\ \Omega_1 c_1 + \Omega_2 c_2 = 1, \\ \nabla \cdot v = \frac{1}{\eta^*} P, \\ c_1 \nabla \mu_1 + c_2 \nabla \mu_2 = 0. \end{cases} \quad (9)$$

Limiting cases of the above system are:

- (1) *Rapid plastic flow (Darken bi-velocity).*
- (2) *No plastic flow.*

Rapid plastic flow. In the **Darken bi-velocity method**, it is assumed that the plastic flow occurs rapidly and $P = \text{const}$, $\nabla P = 0$. Then the system (9) is simplified to

$$\begin{cases} \frac{\partial c_1}{\partial t} = -\nabla \cdot (-B_1 c_1 \nabla \mu_1 + c_1 v), \\ \nabla \cdot (\Omega_1 B_1 c_1 \nabla \mu_1 + \Omega_2 B_2 c_2 \nabla \mu_2 - v) = 0, \\ \Omega_1 c_1 + \Omega_2 c_2 = 1, \\ c_1 \nabla \mu_1 + c_2 \nabla \mu_2 = 0, \end{cases} \quad (10)$$

with the unknowns c_1 , c_2 , v and μ_1 . Consider the case $n = 1$. By Eq. (5), we have

$$\frac{\partial \mu_1}{\partial x} = \frac{RT}{N_1} \theta_1 \frac{\partial N_1}{\partial x}, \quad (11)$$

where the thermodynamic factor $\theta_1 = 1 + \frac{d \ln f_1}{d \ln N_1}$. In view of the Gibbs-Duhem Eq. (7), $\frac{\partial \mu_2}{\partial x}$ can be expressed as

$$\frac{\partial \mu_2}{\partial x} = -\frac{N_1}{N_2} \frac{\partial \mu_1}{\partial x}. \quad (12)$$

Hence the volume continuity equation, Eq. (8), takes the form

$$\frac{\partial}{\partial x} \left(v - RT (\Omega_1 B_1 - \Omega_2 B_2) c \theta_1 \frac{\partial N_1}{\partial x} \right) = 0 \quad (13)$$

and in consequence

$$v = RT (\Omega_1 B_1 - \Omega_2 B_2) c \theta_1 \frac{\partial N_1}{\partial x} + K(t), \quad (14)$$

where $K(t)$ is an arbitrary function. Assume that the domain $\Sigma \subset \mathbb{R}$ is an interval and $\Omega_1 J_1 + \Omega_2 J_2 = 0$ on one boundary of Σ . It implies that $K(t) = 0$ and the interdiffusion flux is as follows:

$$J_1 = -RT (B_1 N_2 + B_2 N_1) \Omega_2 c^2 \theta_1 \frac{\partial N_1}{\partial x}. \quad (15)$$

When $f_1 = 1$ (ideal solution) and $\Omega_1 = \Omega_2 = \Omega = c^{-1}$ one gets the Darken simple relation

$$J_1 = -(N_2 D_1 + N_1 D_2) \frac{\partial c_1}{\partial x}, \quad (16)$$

where the diffusivity $D_i = RT B_i$, $i = 1, 2$.

No plastic flow. If the material velocity is negligible, $v = 0$, there is **no plastic deformation**, and the system (9) is reduced to

$$\begin{cases} \frac{\partial c_1}{\partial t} = -\nabla \cdot (-B_1 c_1 (\nabla \mu_1 + \Omega_1 \nabla P)), \\ \nabla \cdot (\Omega_1 B_1 c_1 (\nabla \mu_1 + \Omega_1 \nabla P) + \Omega_2 B_2 c_2 (\nabla \mu_2 + \Omega_2 \nabla P)) = 0, \\ \Omega_1 c_1 + \Omega_2 c_2 = 1, \\ c_1 \nabla \mu_1 + c_2 \nabla \mu_2 = 0, \end{cases} \quad (17)$$

with the unknowns c_1 , c_2 , P and μ_1 . Consider the case $n = 1$. Reasoning similarly as in the previous situation, for the rapid plastic flow, we get

$$\frac{\partial P}{\partial x} = RT \frac{\Omega_2 B_2 - \Omega_1 B_1}{\Omega_1^2 B_1 N_1 + \Omega_2^2 B_2 N_2} \theta_1 \frac{\partial N_1}{\partial x}. \tag{18}$$

Elementary calculations lead to the relation for the interdiffusion flux

$$J_1 = -RT \frac{B_1 B_2}{\Omega_1^2 B_1 N_1 + \Omega_2^2 B_2 N_2} \Omega_2 \theta_1 \frac{\partial N_1}{\partial x}. \tag{19}$$

If $c = \text{const}$, then

$$J_1 = -D \frac{\partial c_1}{\partial x}, \tag{20}$$

where

$$D = RT \frac{B_1 B_2 \theta_1}{(\Omega_1^2 B_1 N_1 + \Omega_2^2 B_2 (1 - N_1)) c^2}. \tag{21}$$

Moreover if $B_2 \ll B_1$ and $\Omega_1 = \Omega_2 = \Omega = c^{-1}$, then (21) simplifies to

$$D = RT \frac{B_2 \theta_1}{\Omega_1^2 N_1 c^2} = RT \frac{B_2 \theta_1}{N_1} \tag{22}$$

and for an ideal solid solution, for which $f_1 = 1$, we obtain

$$D = \frac{D_2}{N_1}. \tag{23}$$

The above means that, when $v = 0$ then the slower component is rate limiting.

We will consider in this paper the case $n = 1$. If $n \geq 2$, then the number of the equations in (9) (also in Eqs. (2)–(4), (6)) and the unknowns is different so the problem is mathematically badly posed. If $n = 2$ or $n = 3$, Σ is a simply connecting region and $\text{rot } v = 0$, then there exists a scalar potential Φ of the drift v , i.e.,

$$-\nabla \Phi = v \tag{24}$$

(see [49–51]). The same remarks are true for (10) and (17). Such a situation will be studied in the future. Add that existence, uniqueness and some properties of solutions to one-dimensional interdiffusion model with the drift, but without the chemical potentials and pressure, were proved in [52].

3 Formulation of Practical Model

In this section, we consider a mathematical model of the nitrogen transport during the nitriding in one-dimensional case, $n = 1$. The model includes the diffusional and convective transport, stress formation and plastic flow. We will transform the system (9) to a system of two equations with the unknowns y_1 and P . Such a system will be better from a mathematical and numerical point of view.

The **assumptions** are:

1. $s = 2$, $1 \equiv Fe$, $2 \equiv N$, the binary one-dimensional system in $\Sigma = [\Lambda_1(t), \Lambda_2] \subset \mathbb{R}$, free for nitrogen at the left boundary, $x = \Lambda_1(t)$, while the right boundary, $x = \Lambda_2$, is a center of the sample.

2. The diffusing components have various diffusivities ($D_1 \neq D_2$) and various partial molar volumes ($\Omega_1 \neq \Omega_2$), the diffusivities and partial molar volumes are constant, i.e., composition independent.

3. Temperature $T = 723 \text{ K}$.

We introduce new variables

$$y_1 = \Omega_1 c_1, \quad y_2 = \Omega_2 c_2, \quad (25)$$

which are interpreted as volume concentrations. It is clear that

$$y_1 + y_2 = 1, \quad (26)$$

because of the Vegard rule.

3.1 Chemical Potential

The chemical potentials of iron and nitrogen are given by (5), where especially $RT \ln f_2 = -\Omega_2 \sigma_h$, $f_2 = f_2(N_2)$ means the activity coefficient of nitrogen. The hydrostatic stress $\sigma_h = \sigma_h(N_2)$ can be expressed by the compressive residual stress parallel to the surface $\sigma_h = \frac{2}{3} \sigma_{\parallel}$. It can be calculated from the lattice dilatation due to the nitrogen penetration, as it results from the Vegard rule

$$\sigma_h = \frac{2}{3} \frac{E}{1 - \nu_P} \frac{u_0 - u}{u_0}, \quad (27)$$

where E is the Young modulus of Fe (we neglect here a dependence of E on the nitrogen content and assume the value for pure Fe), ν_P is the Poisson ratio, u_0 means the Fe lattice constant and $u = u(N_2) = u_0 + u_1 N_2$ represents a linear dependence of the lattice constant on the nitrogen content. Hence

$$\sigma_h = \frac{2E}{3(\nu_P - 1)} \frac{u_1}{u_0} N_2, \quad (28)$$

where u_0 , u_1 , E , ν_P are known constants. Therefore, the activity coefficient f_2 can be written as

$$f_2 = e^{\frac{E\Omega_2}{RT} \frac{2u_1}{3u_0(1-\nu_P)} N_2}. \quad (29)$$

By Eq. (5), we have

$$\frac{\partial \mu_i}{\partial x} = \frac{RT}{N_i} \theta_i \frac{\partial N_i}{\partial x}, \quad i = 1, 2, \quad (30)$$

where the thermodynamic factors $\theta_i = 1 + \frac{d \ln f_i}{d \ln N_i}$. In view of the Gibbs-Duhem equation we obtain

$$\frac{\partial \mu_1}{\partial x} = -\frac{N_2}{N_1} \frac{\partial \mu_2}{\partial x}. \quad (31)$$

Note that $N_1 + N_2 = 1$, by the definition. Eqs. (30) and (31) imply

$$\theta_1 = \theta_2. \tag{32}$$

It follows from (29), the form of θ_2 and Appendix A that

$$\theta_2 = 1 + \frac{2\Omega_1\Omega_2Eu_1(1-y_1)}{3RTu_0(\nu_P-1)(\Omega_1+(\Omega_2-\Omega_1)y_1)}. \tag{33}$$

In this way, θ_1 can be expressed as a function of y_1 .

3.2 System of Equations

Taking into account the Maxwell solid equation, the following relation holds

$$v(t,x) = \frac{1}{\eta^*} \int_{\Lambda_1(t)}^x P(t,s) ds + K(t), \quad x \in [\Lambda_1(t), \Lambda_2]. \tag{34}$$

Upon assuming that at the right boundary $v(t, \Lambda_2) = 0$, the time-dependant function $K(t)$ can be calculated

$$K(t) = -\frac{1}{\eta^*} \int_{\Lambda_1(t)}^{\Lambda_2} P(t,s) ds \tag{35}$$

and hence the drift velocity is

$$v(t,x) = -\frac{1}{\eta^*} \int_x^{\Lambda_2} P(t,s) ds. \tag{36}$$

In consequence, the first equation in (9) becomes

$$\frac{\partial y_1}{\partial t} = B_1 \frac{\partial}{\partial x} \left(y_1 \left(\frac{\partial \mu_1}{\partial x} + \Omega_1 \frac{\partial P}{\partial x} \right) \right) - \frac{1}{\eta^*} y_1 P + \frac{1}{\eta^*} \frac{\partial y_1}{\partial x} \int_x^{\Lambda_2} P(t,s) ds. \tag{37}$$

Combining the volume continuity equation with the Vegard, Maxwell solid and Gibbs-Duhem equations gives

$$\frac{\partial}{\partial x} \left(\left(B_1 y_1 - B_2 (1 - y_1) \frac{c_1}{c_2} \right) \frac{\partial \mu_1}{\partial x} \right) + \frac{\partial}{\partial x} \left((\Omega_1 B_1 y_1 + \Omega_2 B_2 (1 - y_1)) \frac{\partial P}{\partial x} \right) = \frac{P}{\eta^*}. \tag{38}$$

By Eq. (5), we have

$$\frac{\partial \mu_1}{\partial x} = \frac{RT}{N_1} \theta_1 \frac{\partial N_1}{\partial x}, \tag{39}$$

where the thermodynamic factor $\theta_1 = 1 + \frac{d \ln f_1}{d \ln N_1}$. It follows from Appendix A that:

$$\frac{\partial \mu_1}{\partial x} = \frac{RT\Omega_1}{y_1(\Omega_1 + (\Omega_2 - \Omega_1)y_1)} \theta_1 \frac{\partial y_1}{\partial x} \tag{40}$$

and Eq. (38) becomes

$$S(y_1) \frac{\partial^2 P}{\partial x^2} + \frac{\partial y_1}{\partial x} \frac{\partial P}{\partial x} + QP = G(y_1), \tag{41}$$

where

$$S(y_1) = \frac{\Omega_2 B_2}{\Omega_1 B_1 - \Omega_2 B_2} + y_1,$$

$$Q = -\frac{1}{(\Omega_1 B_1 - \Omega_2 B_2) \eta^*},$$

$$G(y_1) = -RT \frac{\partial}{\partial x} \left(\frac{1}{\Omega_1 + (\Omega_2 - \Omega_1) y_1} \theta_1 \frac{\partial y_1}{\partial x} \right).$$

For detailed derivation of (41) see Appendix B. Hence the system (9) can be written in the form

$$\begin{cases} \frac{\partial y_1}{\partial t} = RT \Omega_1 B_1 \frac{\partial}{\partial x} \left(\frac{1}{\Omega_1 + (\Omega_2 - \Omega_1) y_1} \theta_1 \frac{\partial y_1}{\partial x} \right) + \Omega_1 B_1 \frac{\partial}{\partial x} \left(y_1 \frac{\partial P}{\partial x} \right) \\ \quad - \frac{1}{\eta^*} y_1 P + \frac{1}{\eta^*} \frac{\partial y_1}{\partial x} \int_x^{\Lambda_2} P(t, s) ds, \\ S(y_1) \frac{\partial^2 P}{\partial x^2} + \frac{\partial y_1}{\partial x} \frac{\partial P}{\partial x} + QP = G(y_1), \end{cases} \quad (42)$$

with the unknowns y_1 and P (see (32), (33)).

Eq. (42) is a parabolic-elliptic system of nonlinear nonlocal strongly coupled differential equations on the domain $[\Lambda_1(t), \Lambda_2]$, where $\Lambda_1(t)$ is the solution of the initial value problem

$$\begin{cases} \Lambda_1'(t) = v(t, \Lambda_1(t)), \\ \Lambda_1(0) = 0, \end{cases} \quad (43)$$

that by (36) can be written in the form

$$\begin{cases} \Lambda_1'(t) = -\frac{1}{\eta^*} \int_{\Lambda_1(t)}^{\Lambda_2} P(t, s) ds, \\ \Lambda_1(0) = 0. \end{cases} \quad (44)$$

For the system (42), we formulate the initial condition at $t = 0$,

$$y_1(0, x) = Y(x), \quad x \in [0, \Lambda_2], \quad (45)$$

where Y is a given function. The boundary conditions will be discussed in the next section of the paper.

3.3 Boundary Conditions

For Eq. (42) we give the following mixed boundary conditions BC.

1. At the right boundary, $x = \Lambda_2$, the Neumann BC for y_1 and P ,

$$\begin{cases} \frac{\partial y_1}{\partial x}(t, \Lambda_2) = 0, \\ \frac{\partial P}{\partial x}(t, \Lambda_2) = 0. \end{cases} \quad (46)$$

2. At the left boundary, $x = \Lambda_1(t)$, the Dirichlet BC for P ,

$$P(t, \Lambda_1(t)) = P_L(t), \tag{47}$$

where P_L is a given function.

3. Two types of BC for y_1 are considered at the left boundary, $x = \Lambda_1(t)$: the Dirichlet and the Chang-Jaffé.

(a) The Dirichlet BC

$$y_1(t, \Lambda_1(t)) = Y_L(t), \tag{48}$$

where Y_L is a given function. The question is what Y_L to propose. For this purpose, the surface nitrogen concentration is given by the function [53],

$$N_2^s(t) = N_{2,\infty}^s (1 - e^{-\beta t}), \tag{49}$$

where $N_{2,\infty}^s = \text{const}$ is a surface-nitrogen concentration at $t \rightarrow \infty$ (equilibrium steady-state surface concentration) and β is a constant parameter that tells how fast $N_2^s(t)$ approaches $N_{2,\infty}^s$. For the boundary condition (48) and experimental depth profiles, Christiansen et al. [22] determined, by inverse modeling, the β parameter to be 0.0001. By noting that $y_1 = \Omega_1 N_1 (\Omega_2 - (\Omega_2 - \Omega_1) N_1)^{-1}$ as has been calculated in Appendix A, we get

$$Y_L(t) = \frac{\Omega_1 \varphi(t)}{\Omega_2 - (\Omega_2 - \Omega_1) \varphi(t)}, \tag{50}$$

where $\varphi(t) = 1 - N_{2,\infty}^s (1 - e^{-\beta t})$.

(b) Instead, because the left boundary is open for the nitrogen flux, it is reasonable to consider the boundary as an interface and assume that there is no accumulation of nitrogen “within” it. In such a case, we can write

$$J_2(t, \Lambda_1(t)) = k_f F - k_b c_2(t, \Lambda_1(t)) = k_f F - \frac{k_b}{\Omega_2} y_2(t, \Lambda_1(t)), \tag{51}$$

where k_f, k_b, F are given constants. Equivalently, it can be expressed in the term of y_1 ,

$$J_1(t, \Lambda_1(t)) : = -\frac{\Omega_2 k_f F}{\Omega_1} + \frac{k_b}{\Omega_1} (1 - y_1(t, \Lambda_1(t))), \tag{52}$$

by (26) and Appendix C. In consequence, using (36) and (40), we get

$$\frac{B_1 RT \Omega_1}{\Omega_1 + (\Omega_2 - \Omega_1) y_1} \theta_1 \frac{\partial y_1}{\partial x} + B_1 \Omega_1 y_1 \frac{\partial P}{\partial x} + \frac{1}{\eta^*} y_1 \int_{\Lambda_1(t)}^{\Lambda_2} P(t, s) ds = \Omega_2 k_f F - k_b (1 - y_1) \tag{53}$$

at the points $(t, \Lambda_1(t))$ (see (32), (33)). The above formula is called the non-local Chang-Jaffé BC.

3.4 Data and Results

For the system (37)–(41), the set of data have been applied, Tab. 1. Constant diffusivities (mobilities), i.e., concentration independent, have been used. Most of the computations have been made assuming for *Fe* the highest diffusivity in the α phase (equal to the lowest diffusivity in the γ phase) [54]. For this diffusivity, a plateau appears at the nitrogen concentration profile, Figs. 1–3, 5–7, which is according to the expectations. Such a choice agrees with the supposition that the diffusion in the expanded austenite is faster than it is expected from chemical diffusion [18].

Table 1: The data used in the simulations

	Temperature T [K]	723
<i>Fe</i> elastic constants	Lenght L [m]	0.00005
	Young modulus ¹ E [Pa]	$2 \cdot 10^{11}$
	Poisson number ν_P [-]	0.33
Partial molar volumes	Ω_1^2 [m ³ /mol]	$7.09 \cdot 10^{-6}$
	Ω_2^3 [m ³ /mol]	$4.24 \cdot 10^{-6}$
Thermodynamic pressure	u_0 [m] ⁴	$2.86 \cdot 10^{-10}$
	u_1 [m] ⁵	$0.60 \cdot 10^{-10}$
Mobilities	B_1^6 [mol · s/kg]	$8.32 \cdot 10^{-21}$
Viscosity coefficient	B_2^7 [mol · s/kg]	$3.6 \cdot 10^{-20}$
	η , [Pa · s]-experimental ⁸	$2.5 \cdot 10^3$
	η , [Pa · s]-calculated ⁹	$1.8 \cdot 10^4 \div 10^{11}$
Initial and boundary conditions	$Y(x)$ [-]	1
	$N_{2,\infty}^s$ [at.%]	0.25
	$P_L(t)$ [Pa]	0
	$k_f \left[\frac{\text{mol}}{\text{m}^2 \cdot \text{s}} \right]^{10}$	$0.5 \cdot 10^{-9}$
	$k_b \left[\frac{\text{mol}}{\text{m}^2 \cdot \text{s}} \right]^{10}$	$0.5 \cdot 10^{-9}$
	$F \left[\frac{\text{mol}}{\text{m}^3} \right]^{10}$	$6.0 \cdot 10^3$

Notes:

¹Reference [55]; ²Reference [56]; ³Reference [57]; ⁴Reference [58]; ⁵Reference [59]; ⁶Highest mobility in the α phase, Reference [54];

⁷Reference [60]; ⁸Reference [61]; ⁹Calculated from Eq. (54); ¹⁰Fitted to $N_{2,\infty}^s = 0.25$ at.%.

To study an effect of viscosity on the nitrogen transport, we have made the simulations for the experimentally found viscosity coefficient, $2.5 \cdot 10^3 \text{ Pa} \cdot \text{s}$ (see [61]) and repeated them for the two extreme values calculated theoretically for the pure *Fe* and *Fe* with 0.25 *N* at.%; $1.8 \cdot 10^4$ and $10^{11} \text{ Pa} \cdot \text{s}$, respectively. In calculations of these extreme viscosity coefficients, the Stokes-Einstein relation, which combines the viscosity with diffusivity has been used. For the binary system it is [43]:

$$\eta = \frac{cd^2RT}{\gamma D_{NP}}, \quad (54)$$

where $c = \Omega^{-1}$, d is a distance between the atoms, D_{NP} is the Nernst-Planck interdiffusion coefficient and γ is a geometric factor, $\gamma \approx 10$. An effect of a sample thickness on the stress distribution and concentration profiles has been also studied and the simulations have been repeated for 4 different sample thicknesses. Besides, the computations for various boundary conditions have been made.

The programming has been performed using the Chesbyshev-Gauss-Lobatto and power grids. In Fig. 1, we show that the results don't depend on the choice of the grid. Therefore, we have arbitrarily decided to perform the remaining computation using the program based on the power grid.

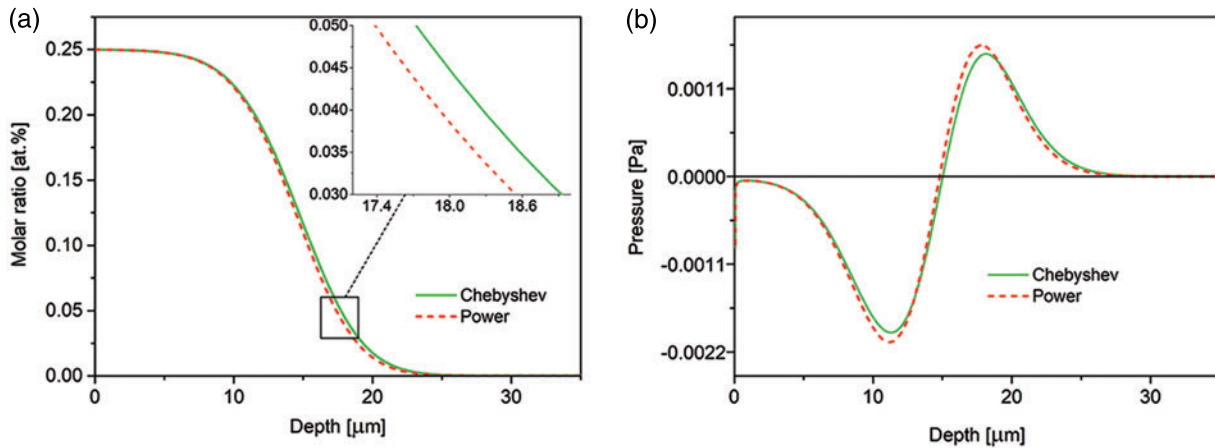


Figure 1: Comparison of the nitrogen concentration-depth profiles (a) and spatial pressure distribution (b), computed using the Chesbyshev-Gauss-Lobatto and power grids. The results after 15 h of the nitriding. The data simulated for the Dirichlet BC and experimental viscosity coefficient

In Fig. 2a comparison of simulations made for the two types of boundary conditions for nitrogen concentration at the open boundary is presented. We consider the Dirichlet and Chang-Jaffé boundary conditions. Although in the case of the Chang-Jaffé condition, the nitrogen concentration at the open boundary is calculated in the self-consistent way, without assuming given values, the both curves clearly overlap. The results also show that the concentration profile after 30 min of the processing exhibits an inflection, which at longer times transforms into a plateau characteristic for the non-Fickian diffusion in the expanded austenite.

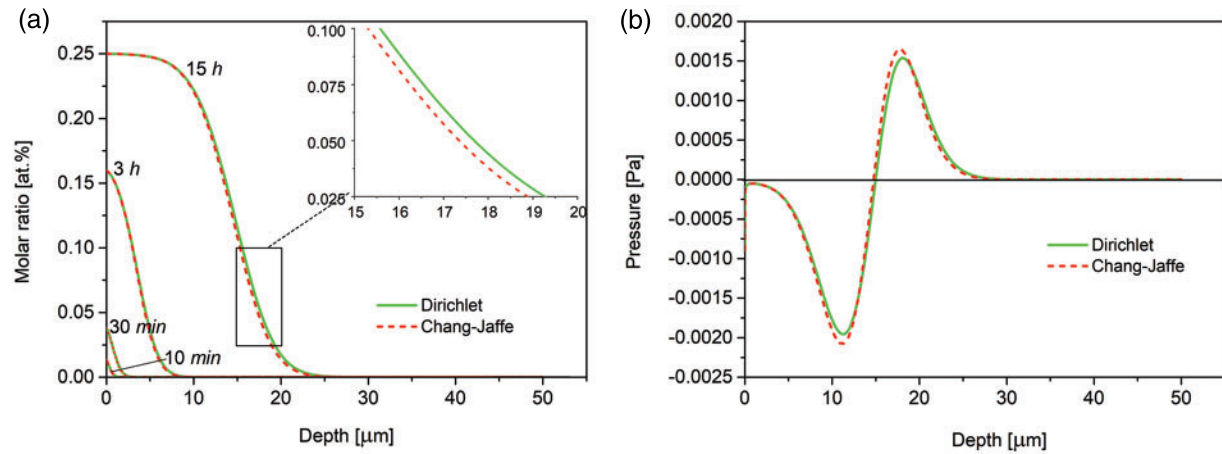


Figure 2: (a) Time evolution of the nitrogen concentration-depth profiles simulated with the use of the Dirichlet and Chang-Jaffé boundary conditions for the nitrogen concentration at the free left boundary $\Lambda_1(t)$; (b) spatial pressure distribution after 15 h of the processing. The data for the experimental viscosity coefficient

An effect of partial molar volume (here partial molar volume of nitrogen) is presented in Fig. 3, where we show the nitrogen concentration and pressure after 15 h of the processing. The assumed values are: $\Omega_2 = 4.24 \cdot 10^{-6} \text{ m}^3/\text{mol}$ —according to Jespersen [57] and $\Omega_2 = 1.73 \cdot 10^{-5} \text{ m}^3/\text{mol}$ —according to ChemGlobe. It is seen that the variation of the Ω_2 affects mainly a case depth while the characteristic plateau does not disappear. This fact confirms the validity of our model.

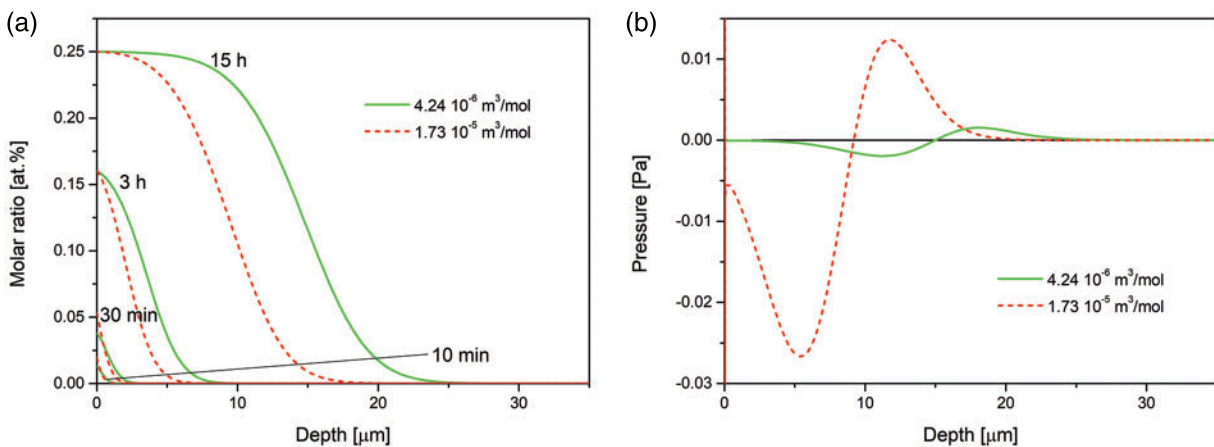


Figure 3: (a) Time evolution of the nitrogen concentration-depth profiles simulated for the nitrogen partial molar volume $\Omega_2 = 4.24 \cdot 10^{-6} \text{ m}^3/\text{mol}$ given in [57], and the nitrogen partial molar volume $\Omega_2 = 1.73 \cdot 10^{-5} \text{ m}^3/\text{mol}$ given in <https://chemglobe.org/ptoe/>; (b) spatial pressure distribution after 15 h of the processing. The data simulated for the Dirichlet BC and experimental viscosity coefficient

When we assume the Fe mobility equal to that at 723 K [54], $B_1 = 1.66 \cdot 10^{-22}$ mol · s/kg, the results are qualitatively different. The plateau disappears and the sample becomes elongated, Fig. 4. Pressure distribution is also qualitatively different. It is because the computational time is too short for such a small mobility B_1 . For the plateau to appear, the time would have to be around 1500 h.

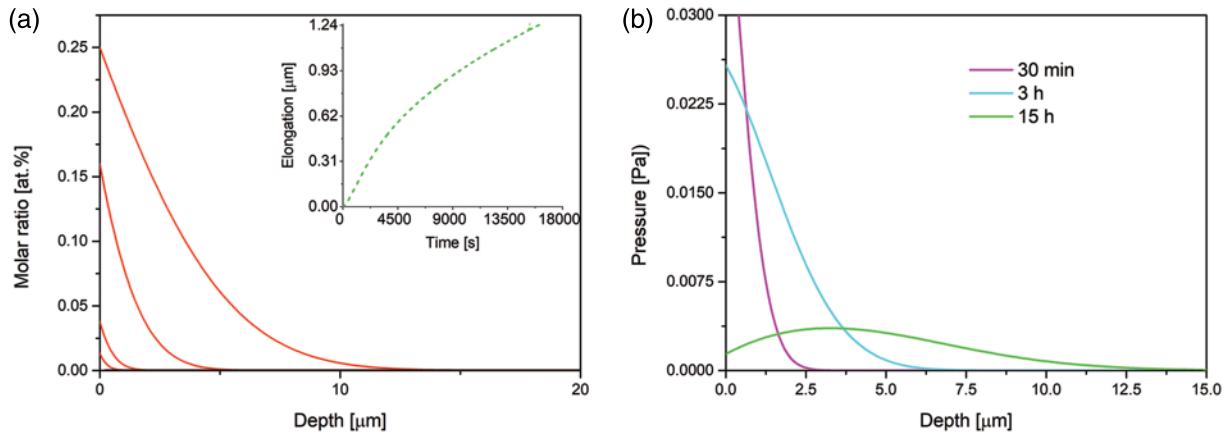


Figure 4: Time evolution of the nitrogen concentration-depth profiles (a) and spatial pressure distribution (b), simulated for $B_1 = 1.66 \cdot 10^{-22}$ mol · s/kg (the Fe mobility in 723 K). The profiles after 10, 30 min, 3 and 15 h of the nitriding. The data simulated for the Dirichlet BC and experimental viscosity coefficient

In Fig. 5, the results for 4 samples of different thicknesses are presented. It is seen that the amount of the nitrogen dissolved and the case depth decrease when the layer thickness increases, Figs. 5e–5f. The observed differences are due to various stress distribution in the samples of various thicknesses. The pressure changing with the depth (pressure gradient) implies an additional driving force for the diffusion. It is seen that the pressure gradient decreases at longer times.

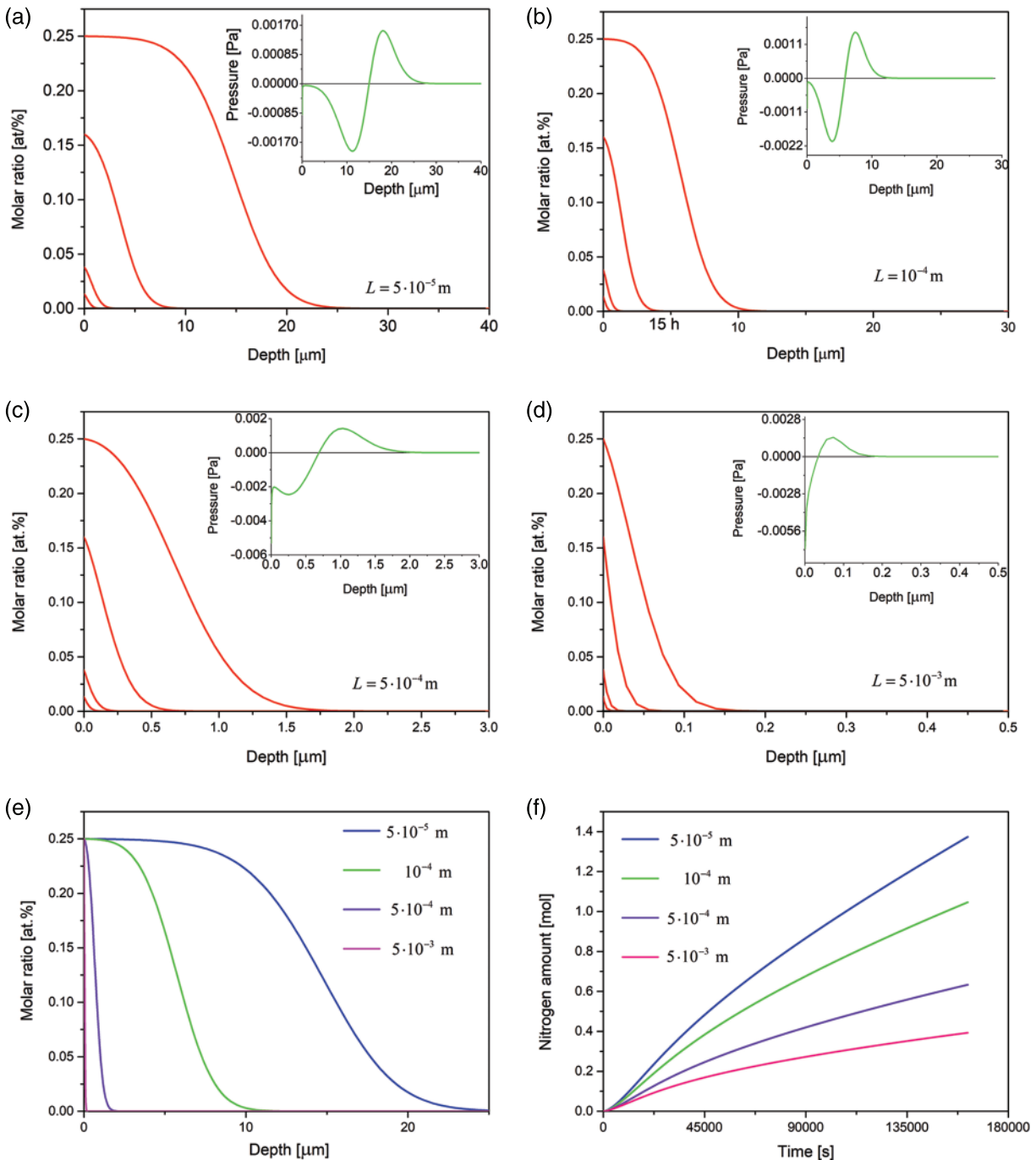


Figure 5: (a–d) Time evolution of the nitrogen concentration together with the spatial pressure distribution (in insets) simulated for the samples of various thicknesses, the respective profiles after 10, 30 min, 3 and 15 h of the nitriding; (e) comparison of nitrogen concentration profiles after 15 h of the nitriding of the samples of various thicknesses; (f) amount of nitrogen dissolved in the samples vs. time. The data simulated for the Dirichlet BC and experimental viscosity coefficient

Only quantitative differences are seen when the final nitrogen concentration at the open boundary is increased from 0.25 at.% to 0.35 at.%, Fig. 6.

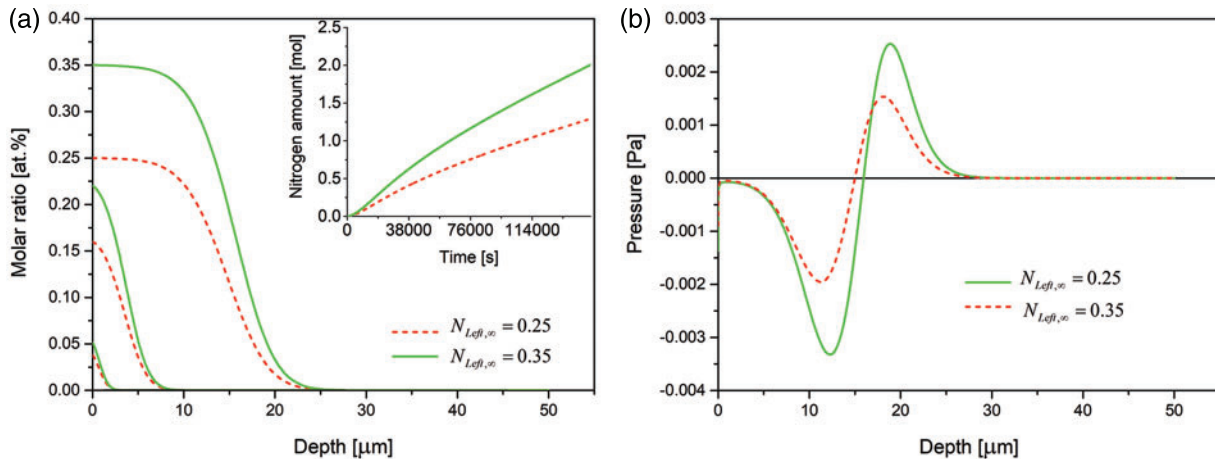


Figure 6: (a) Time evolution of the nitrogen concentration together with nitrogen dissolved (in inset) and (b) spatial pressure distribution for various steady-state nitrogen concentrations at the free left boundary $\Lambda_1(t)$, 0.25 and 0.35 at.%. The respective profiles after 30 min, 3 and 15 h of the nitriding. The data simulated for the Dirichlet BC and experimental viscosity coefficient

The effect of viscosity coefficient is presented in Fig. 7. It is seen that with increasing viscosity coefficient the case depth decreases and less nitrogen is dissolved in the substrate.

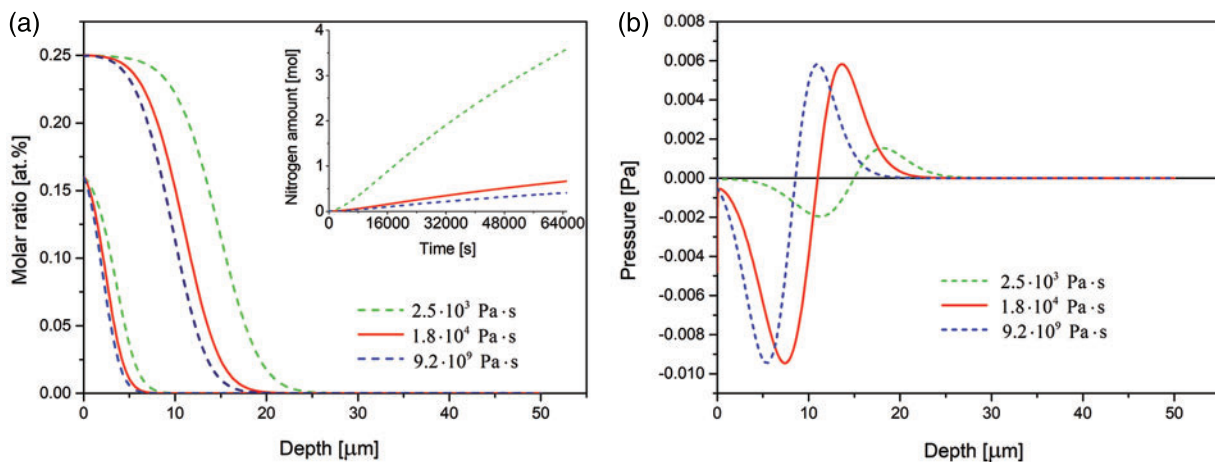


Figure 7: (a) Time evolution of the nitrogen concentration together with nitrogen dissolved (in inset) and (b) spatial pressure distribution simulated for the 3 samples of various viscosity coefficients. The respective profiles after 3 and 15 h of the nitriding. The data simulated for the Dirichlet BC

The presented results show that the appearance of the plateau at the nitrogen concentration profiles is conditioned by the mobilities of the species. It appears when the Fe mobility is higher than that at 723 K. Such processing can be realized in plasma conditions. The sample elongation is not observed. Qualitatively different results are obtained when assuming Fe mobility at 723 K (about 5 orders lower). No plateau appears and the sample becomes elongated. The characteristic plateau-type shape of the N -concentration depth profile has been confirmed by many authors [4,21,28]. Christiansen et al. in [20–22,28] studied the effects of in-depth stress gradients in expanded austenite. The obtained profiles showed a clear plateau followed by a steep nitrogen concentration decrease. Our results agree well with these results. Also, the experimental data measured by electron probe microanalysis (EPMA) in AISI 316 steel after low-temperature nitriding (440°C) for 23 hours at the nitriding potential $K_N = 1.41 \text{ bar}^{-1/2}$ (at which the surface nitrogen concentration is 0.25 at.%) and presented in [22] (Fig. 4) show the validity of the calculated profiles. By comparing the thickness of the nitride zone, our simulation provides an overestimate. The validity can be improved by adopting concentration-dependent diffusivity.

4 Summary and Conclusions

Low and intermediate-temperature nitriding of iron and stainless steel can cause a formation of expanded austenite phase. In this research, a formation of expanded austenite is modeled using the Darken *bi*-velocity method combined with the Vegard rule, the Maxwell model of viscoelastic solid, and the Gibbs-Duhem equation. It is the first such approach, which takes into account the interdiffusion of all components in the solid alloy. The model is formulated in any dimension and is given by a differential-algebraic system of 5 equations. In the one dimensional case, this system is equivalently transformed to the differential system of 2 equations only, which from analytical point of view is better to be studied. Effective mixed type boundary conditions are given. Such a nonlinear strongly coupled parabolic-elliptic differential initial-boundary Stefan type problem is solved numerically. A series of simulations is made. The results confirm an appearance of the characteristic plateau on the nitrogen concentration-depth profiles which is in agreement with literature data (see for example [20–22,28]). The model can be improved by the way of using concentration dependent diffusivities. It can be concluded that:

- The nitrogen transport during nitriding is advanced by means of the stress and strain assisted interdiffusion.
- The stress enhances the diffusion.
- The interdiffusion can cause an imbalance in the volume transport and a non-uniform stress-free strain.
- The stress and strain depend on the components' mobilities, viscosity coefficient and thickness of the substrate.
- Relaxation of the internal stresses generated by unbalanced diffusion fluxes can become the rate-limiting step for the interdiffusion.

The Maxwell model is usually applied to the case of small deformations. For the large deformations one should include non-linearity, e.g., the upper-convected Maxwell model. It can be further improved by the way of using concentration dependent diffusivities.

The initial boundary value problem presented here can be extended and even used in practical applications.

Funding Statement: This work has been supported by the National Science Center (Poland) Decision No. UMO-2013/11/B/ST8/03758 and by the Faculty of Applied Mathematics AGH

UST statutory tasks within subsidy of Ministry of Science and Higher Education (Grant No. 16.16.420.054). Research data are referenced in [Section 3.4](#). They will be available on requirements.

Conflicts of Interest: The authors declare that they have no conflicts of interest to report regarding the present study.

References

1. Pye, D. (2003). *Practical nitriding and ferritic nitrocarburizing*. Geauga County, Ohio: ASM International.
2. Somers, M., Christiansen, T. (2014). Low-temperature surface hardening of stainless steels. In: *ASM Handbook volume 4D: Heat treating of irons and steels*. USA: ASM International.
3. Mittemeijer, E., Somers, M. (2015). Thermochemical surface engineering of steels, surface engineering, part three: Nitriding, nitrocarburizing and carburizing. In: Mittemeijer, E., Somers, M. (Eds.), *Woodhead publishing series in metals and surface engineering*. Amsterdam, Netherlands: Elsevier.
4. Du, H., Somers, M., Agren, J. (2000). Microstructural and compositional evolution of compound layers during gaseous nitrocarburizing. *Metallurgical and Materials Transactions A*, 31, 195–211. DOI 10.1007/s11661-000-0065-7.
5. Somers, M., Mittemeijer, E. (1998). Modeling the kinetics of the nitriding and nitrocarburizing of iron. *17th Heat Treating Society Conference Proceedings*. pp. 321–330. Metals Park, ASM International.
6. Lebrun, J. (2015). Plasma-assisted processes for surface hardening of stainless steel. In: Mittemeijer, E. J., Somers, M. A. J. (Eds.), *Thermochemical surface engineering of steels, woodhead publishing*, pp. 615–632. Amsterdam, Netherlands: Elsevier.
7. Somers, M., Christiansen, T. (2015). Low temperature surface hardening of stainless steel. In: Mittemeijer, E. J., Somers, M. A. J. (Eds.), *Thermochemical surface engineering of steels, woodhead publishing*, pp. 557–579. Amsterdam, Netherlands: Elsevier.
8. Kovács, D., Quintana, I., Dobránszky, J. (2019). Effects of different variants of plasma nitriding on the properties of the nitrided layer. *Journal of Materials Engineering and Performance*, 28, 5485–5493. DOI 10.1007/s11665-019-04292-9.
9. Naeem, M., Shafiq, M., ul Islam, M. Z., Nawaz, N., Daz-Guillén, J. et al. (2016). Effect of cathodic cage size on plasma nitriding of AISI 304 steel. *Material Letters*, 181, 78–81. DOI 10.1016/j.matlet.2016.05.144.
10. Corujeira-Gallo, S., Dong, H. (2009). On the fundamental mechanisms of active screen plasma nitriding. *Vacuum*, 84(2), 321–325. DOI 10.1016/j.vacuum.2009.07.002.
11. Ahangarani, S., Mahboubi, F., Sabour, A. (2006). Effects of various nitriding parameters on active screen plasma nitriding behavior of a low-alloy steel. *Vacuum*, 80(9), 1032–1037. DOI 10.1016/j.vacuum.2006.01.013.
12. Li, Y., He, Y., Wang, W., Mao, J., Zhang, L. et al. (2018). Plasma nitriding of aisi, 304 stainless steel in cathodic and floating electric potential: Influence on morphology, chemical characteristics and tribological behavior. *Journal of Materials Engineering and Performance*, 27(3), 948–960. DOI 10.1007/s11665-018-3199-8.
13. Kücükyıldız, Ö., Grumsen, F., Christiansen, T., Winther, G., Somers, M. (2020). Anisotropy effects on gaseous nitriding of austenitic stainless steel single crystals. *Acta Materialia*, 194, 168–177. DOI 10.1016/j.actamat.2020.04.062.
14. Mehedi, M., Jiang, Y., Ma, B., Wang, J. (2019). Nitriding and martensitic phase transformation of the copper and boron doped iron nitride magnet. *Acta Materialia*, 167, 80–88. DOI 10.1016/j.actamat.2019.01.034.
15. Tao, X., Matthews, A., Leyland, A. (2020). On the nitrogen-induced lattice expansion of a non-stainless austenitic steel, invar 36, under triode plasma nitriding. *Metallurgical and Materials Transactions A*, 51, 436–447. DOI 10.1007/s11661-019-05526-0.
16. Cavaliere, P., Zavarise, G., Perillo, M. (2009). Modeling of the carburizing and nitriding processes. *Computational Materials Science*, 46, 26–35. DOI 10.1016/j.commatsci.2009.01.024.

17. Buchhagen, P., Bell, T. (1996). Simulation of the residual stress development in the diffusion layer of low alloy plasma nitride steels. *Computational Materials Science*, 7, 228–234. DOI 10.1016/S0927-0256(96)00085-7.
18. Galdikas, A., Moskaliuviene, T. (2010). Stress induced nitrogen diffusion during nitriding of austenitic stainless steel. *Computational Materials Science*, 50, 796–799. DOI 10.1016/j.commatsci.2010.10.018.
19. Kamminga, J., Janssen, G. (2006). Calculation of nitrogen depth profiles in nitride multi-component ferritic steel. *Surface and Coating Technology*, 200, 5896–5901. DOI 10.1016/j.surfcoat.2005.09.002.
20. Jespersen, F., Hattel, J., Somers, M. (2016). Modelling the evolution of composition-and stress-depth profiles in austenitic stainless steels during low-temperature nitriding. *Modelling and Simulation in Material Science and Engineering*, 24(2), 025003. DOI 10.1088/0965-0393/24/2/025003.
21. Christiansen, T., Somers, M. (2006). Avoiding ghost stress on reconstruction of stress-and composition-depth profiles from destructive x-ray diffraction depth profiling. *Materials Science and Engineering A*, 424, 181–189. DOI 10.1016/j.msea.2006.03.007.
22. Christiansen, T., Dahl, K., Somers, M. (2008). Nitrogen diffusion and nitrogen depth profiles in expanded austenite: experimental assessment, numerical simulation and role of stress. *Materials Science and Technology*, 24, 159–167. DOI 10.1179/026708307X232901.
23. Larish, B., Brusky, V., Spies, H. (1999). Plasma nitriding of stainless steels at low temperatures. *Surface and Coatings Technology*, 116–119, 205–211. DOI 10.1016/S0257-8972(99)00084-5.
24. Menthe, E., Rie, K. (1999). Further investigation of the structure and properties of austenitic stainless steel after plasma nitriding. *Surface and Coatings Technology*, 116–119, 199–204. DOI 10.1016/S0257-8972(99)00085-7.
25. Somers, M., Christiansen, T. (2015). Low temperature surface hardening of stainless steel. In: Mittemeijer, E. J., Somers, M. A. J. (Eds.), *Thermochemical surface engineering of steels, surface engineering, part four: low temperature carburizing and nitriding*, woodhead publishing, series in metals and surface engineering. Amsterdam, Netherlands: Elsevier.
26. Borgioli, F. (2020). From austenitic stainless steel to expanded austenite s phase: formation, characteristics and properties of an elusive metastable phase. *Metals*, 10(2), 187. DOI 10.3390/met10020187.
27. Keddami, M., Thiriet, T., Marcos, G., Czerwicz, T. (2017). Characterization of the expanded austenite developed on aisi 316 lm steel by plasma nitriding. *Journal of Mining and Metallurgy Section B Metallurgy*, 53(1B), 47–52. DOI 10.2298/JMMB151115026K.
28. Christiansen, T., Hummelshj, T., Somers, M. (2010). Expanded austenite, crystallography and residual stress. *Surface Engineering*, 26, 242–247. DOI 10.1179/026708410X12506870724316.
29. Ichii, K., Fujimura, K., Takase, T. (1986). Structure of the ion-nitrided layer of 18-8 stainless steel. *Technology Reports of Kansai University*, 27, 135–144.
30. Zhang, Z., Bell, T. (1985). Structure and corrosion resistance of plasma nitrided stainless steel. *Surface Engineering*, 1, 131–136. DOI 10.1179/sur.1985.1.2.131.
31. Czerwicz, T., He, H., Marcos, G., Thiriet, T., Weber, S. et al. (2009). Fundamental and innovations in plasma assisted diffusion of nitrogen and carbon in austenitic stainless steels and related alloys. *Plasma Processes and Polymers*, 6, 401–409. DOI 10.1002/ppap.200930003.
32. Dong, H. (2010). S-phase surface engineering of fe-cr, co-cr and ni-cr alloys. *International Materials Reviews*, 55, 65–98. DOI 10.1179/095066009X12572530170589.
33. Somers, M., Kücüküydiz, Ö., Ormstrup, C., Alimadadi, H., Hattel, J. et al. (2018). Residual stress in expanded austenite on stainless steel; origin, measurement, and prediction. *Materials Performance and Characterisation*, 7, 693–716. DOI 10.1520/MPC20170145.
34. Fernandes, F., Christiansen, T., Winther, G., Somers, M. (2017). Measurement and tailoring of residual stress in expanded austenite on austenitic stainless steel. *Materials Science and Engineering A*, 701, 167–173. DOI 10.1016/j.msea.2017.06.082.
35. Brink, B., Ståhl, K., Christiansen, T., Oddershede, J., Somers, M. (2017). On the elusive crystal structure of expanded austenite. *Scripta Materialia*, 131, 59–62. DOI 10.1016/j.scriptamat.2017.01.006.

36. Piekoszewski, J., Sartowska, B., Walis', L., Werner, Z., Kopcewicz, M. et al. (2004). Interaction of nitrogen atoms in expanded austenite formed in pure iron by intense nitrogen plasma pulses. *NUKLEONIKA*, 49, 57–60.
37. Piekoszewski, J., Langner, J., Białoskórski, J., Kozłowska, B., Pochrybniak, C. et al. (1993). Introduction of nitrogen onto metals by high intensity pulsed ion beams. *Nuclear Instruments and Methods in Physics Research Section B*, 80–81, 344–347. DOI 10.1016/0168-583X(93)96138-3.
38. Williamson, D. L., Ivanov, I., Wei, R., Wilbur, P. (1991). Role of chromium in high-dose, high-rate, elevated temperature nitrogen implantation of austenitic stainless steels. *MRS Online Proceedings Library*, 235, 473–478. DOI 10.1557/PROC-235-473.
39. Parascandola, S., Möller, W., Williamson, D. (2000). The nitrogen transport in austenitic stainless steel at moderate temperatures. *Applied Physics Letters*, 76, 2194–2196. DOI 10.1063/1.126294.
40. Galdikas, A., Moskaliuviene, T. (2013). Swelling effect on stress induced and concentration dependent diffusion of nitrogen in plasma nitrided austenitic stainless steel. *Computational Materials Science*, 72, 140–145. DOI 10.1016/j.commatsci.2013.02.007.
41. Kücükyıldız, Ö. C., Sonne, M. R., Thorborg, J., Somers, M. A. J., Hattel, J. H. (2020). Thermo-chemical-mechanical simulation of low temperature nitriding of austenitic stainless steel; inverse modelling of surface reaction rates. *Surface and Coatings Technology*, 381, 125145. DOI 10.1016/j.surfcoat.2019.125145.
42. Stephenson, G. (1986). Plastic strain and stress during interdiffusion. *Scripta Metallurgica*, 20(4), 465–470. DOI 10.1016/0036-9748(86)90237-1.
43. Stephenson, G. (1988). Deformation during interdiffusion. *Acta Metallurgica*, 36(10), 2663–2683. DOI 10.1016/0001-6160(88)90114-9.
44. Tkacz-Śmiech, K., Bożek, B., Sapa, L., Danielewski, M. (2017). Viscosity controlled interdiffusion in nitriding. *Diffusion Foundations*, 10, 28–38. DOI 10.4028/www.scientific.net/DF.10.28.
45. Larche, F., Cahn, J. (1985). The interactions of composition and stress in crystalline solids. *Acta Metallurgica*, 33, 331–357. DOI 10.1016/0001-6160(85)90077-X.
46. Darken, L. S. (1948). Diffusion, mobility and their interrelation through free energy in binary metallic systems. *Transactions of the Metallurgical Society of AIME*, 175, 184–201. DOI 10.1007/s11661-010-0177-7.
47. Darken, L. S. (1949). Diffusion of carbon in austenite with a discontinuity of composition. *Transactions of the Metallurgical Society of AIME*, 180, 430–438.
48. Danielewski, M., Wierzba, B. (2010). Thermodynamically consistent bi-velocity mass transport phenomenology. *Acta Materialia*, 58, 6717–6727. DOI 10.1016/j.actamat.2010.08.037.
49. Sapa, L., Bożek, B., Tkacz-Śmiech, K., Zajusz, M., Danielewski, M. (2020). Interdiffusion in many dimensions: Mathematical models, numerical simulations and experiment. *Mathematics and Mechanics of Solids*, 25(12), 2178–2198. DOI 10.1177/1081286520923376.
50. Sapa, L., Bożek, B., Danielewski, M. (2018). Weak solutions to interdiffusion models with vegard rule. *Book Series: AIP Conference Proceedings 1926, 6th International Eurasian Conference on Mathematical Sciences and Applications*, pp. 0200391–0200399. USA: AIP Publishing.
51. Bożek, B., Sapa, L., Danielewski, M. (2019). Difference methods to one and multidimensional interdiffusion models with vegard rule. *Mathematical Modelling and Analysis*, 24(2), 276–296. DOI 10.3846/mma.2019.018.
52. Sapa, L., Bożek, B., Danielewski, M. (2018). Existence, uniqueness and properties of global weak solutions to interdiffusion with vegard rule. *Topological Methods in Nonlinear Analysis*, 52(2), 432–448. DOI 10.12775/TMNA.2018.008.
53. Crank, J. (1975). *The mathematics of diffusion*. Oxford, UK: Oxford University Press.
54. Mehrer, H. (2007). *Diffusion in solids*. Berlin, Germany: Springer.
55. Benito, J., Manero, J., Jorba, J., Roca, A. (2005). Change of Young's modulus of cold-deformed pure iron in a tensile test. *Metallurgical and Materials Transactions A*, 36, 3317–3324. DOI 10.1007/s11661-005-0006-6.
56. Robie, R., Bethke, P. (1962). Molar volumes and densities of minerals. Report TEI-822: United States Department of the Interior Geological Survey.

57. Jespersen, F. (2015). *Interaction of stress and phase transformations during thermochemical surface engineering*. (Ph.d. Thesis). Technical University of Denmark.
58. Davey, W. (1925). Precision measurements of the lattice constants of twelve common metals. *Physical Review*, 25, 753–761. DOI 10.1103/PhysRev.25.753.
59. Liapina, T., Leineweber, A., Mittemeijerand, E., Kockelmann, W. (2004). The lattice parameters of ϵ -iron nitrides: Lattice strains due to a varying degree of nitrogen ordering. *Acta Materialia*, 52, 173–180. DOI 10.1016/j.actamat.2003.09.003.
60. Georgiev, J., Anestiev, L. (1998). Determination of the nitrogen diffusion coefficient in steels with non-isothermal experiments. *Zeitschrift für Metallkunde*, 89(6), 411–416.
61. Savenkov, G., Meshcheryakov, Y. (2002). Structural viscosity of solids. *Combustion, Explosion, and Shock Waves*, 38, 352–357. DOI 10.1023/A:1015614106081.

Appendix A

To express the chemical potential gradient $\frac{\partial \mu_1}{\partial x}$ as a function of y_1 , let us notice first that $N_1 = \frac{c_1}{c}$, $y_1 = \Omega_1 c_1$, $\Omega_1 c_1 + \Omega_2 c_2 = 1$ and $c_1 + c_2 = c$. We can write:

$$c = \frac{\Omega_1 + (\Omega_2 - \Omega_1) y_1}{\Omega_1 \Omega_2}, \tag{55}$$

$$N_1 = \frac{\Omega_1 c_1}{\Omega_1 c} = \frac{y_1}{\Omega_1 c} = \frac{\Omega_2 y_1}{\Omega_1 + (\Omega_2 - \Omega_1) y_1}, \tag{56}$$

$$\frac{\partial N_1}{\partial x} = \frac{\Omega_1 \Omega_2}{(\Omega_1 + (\Omega_2 - \Omega_1) y_1)^2} \frac{\partial y_1}{\partial x}. \tag{57}$$

After introducing (56) and (57) into (39) leads to (40).

Appendix B

We want to find a differential equation on the pressure P . The formulas (38) and (40) imply the relation

$$\begin{aligned} & \frac{\partial}{\partial x} \left(\left(B_1 y_1 - B_2 (1 - y_1) \frac{c_1}{c_2} \right) \frac{RT \Omega_1}{y_1 (\Omega_1 + (\Omega_2 - \Omega_1) y_1)} \theta_1 \frac{\partial y_1}{\partial x} \right) + \frac{\partial}{\partial x} \left((\Omega_1 B_1 - \Omega_2 B_2) y_1 \frac{\partial P}{\partial x} + \Omega_2 B_2 \frac{\partial P}{\partial x} \right) \\ & = \frac{1}{\eta^*} P. \end{aligned} \tag{58}$$

It follows from elementary calculations that

$$B_1 y_1 - B_2 (1 - y_1) \frac{c_1}{c_2} = B_1 y_1 - B_2 (1 - y_1) \frac{c_1 \Omega_1 \Omega_2}{c_2 \Omega_1 \Omega_2} = \frac{\Omega_1 B_1 - \Omega_2 B_2}{\Omega_1} y_1. \tag{59}$$

By inserting (59) to (58) we have

$$\begin{aligned} & RT (\Omega_1 B_1 - \Omega_2 B_2) \frac{\partial}{\partial x} \left(\frac{1}{\Omega_1 + (\Omega_2 - \Omega_1) y_1} \theta_1 \frac{\partial y_1}{\partial x} \right) \\ & + (\Omega_2 B_2 + (\Omega_1 B_1 - \Omega_2 B_2) y_1) \frac{\partial^2 P}{\partial x^2} + (\Omega_1 B_1 - \Omega_2 B_2) \frac{\partial y_1}{\partial x} \frac{\partial P}{\partial x} = \frac{1}{\eta^*} P \end{aligned} \tag{60}$$

and equivalently

$$\begin{aligned} & \left(\frac{\Omega_2 B_2}{\Omega_1 B_1 - \Omega_2 B_2} + y_1 \right) \frac{\partial^2 P}{\partial x^2} + \frac{\partial y_1}{\partial x} \frac{\partial P}{\partial x} - \frac{1}{(\Omega_1 B_1 - \Omega_2 B_2) \eta^*} P \\ & = -RT \left(\frac{\theta_1}{\Omega_1 + (\Omega_2 - \Omega_1) y_1} \frac{\partial^2 y_1}{\partial x^2} + \frac{\partial}{\partial x} \left(\frac{\theta_1}{\Omega_1 + (\Omega_2 - \Omega_1) y_1} \right) \frac{\partial y_1}{\partial x} \right). \end{aligned} \tag{61}$$

In fact Eq. (61) is identical with Eq. (41).

Appendix C

We will show that

$$\Omega_1 J_1 + \Omega_2 J_2 = 0. \tag{62}$$

It follows from (8) that

$$\Omega_1 J_1 + \Omega_2 J_2 = K(t), \quad (63)$$

by one dimension $n = 1$. Let $J_i^d = -B_i c_i \left(\frac{\partial \mu_i}{\partial x} + \Omega_i \frac{\partial P}{\partial x} \right)$ mean the diffusion terms of the fluxes J_i , $i = 1, 2$ given in (1). Because at the right boundary $v(t, \Lambda_2) = 0$ and $\Omega_1 J_1^d(t, \Lambda_2) + \Omega_2 J_2^d(t, \Lambda_2) = 0$, then $K(t) \equiv 0$ and in consequence (62) is satisfied.

Appendix D

We will construct implicit finite difference methods for the system (42) with the initial condition (45) and two types of boundary conditions: (46)–(48)-the Robin type, and (46), (47), (53)-the generalized non-local Robin type, respectively. These numerical methods are generated by some linearization and splitting ideas. The data used in simulations are given in Table 1. To avoid a double indexation, we put: $y: = y_1$ and $\theta: = \theta_1$.

Define a mesh on the set $[0, \infty) \times \Sigma(t) = [\Lambda_1(t), \Lambda_2]$ in the following way. Let $\tau > 0$ stands for the time step of the mesh and define nodal time points $t^\nu = \nu\tau$, $\nu \in \mathbb{N} \cup \{0\}$. Let moreover $M \in \mathbb{N}$ be given, $\Lambda_1^\nu = x_0^\nu < x_1^\nu < \dots < x_M^\nu < x_{M+1}^\nu = \Lambda_2$ be at this moment arbitrarily fixed nodal space points and let $h_m^\nu = x_m^\nu - x_{m-1}^\nu$, $m = 1, \dots, M+1$ mean the space steps of the mesh. Define new nodal space points $\bar{x}_m^\nu = x_m + \frac{1}{2}h_{m+1}$, $m = 0, \dots, M$. Note that $\bar{x}_m^\nu - \bar{x}_{m-1}^\nu = \frac{h_m + h_{m+1}}{2}$. Put $\bar{h}_m^\nu = \frac{h_m + h_{m+1}}{2}$.

For the left end of the domain $\Sigma(t)$, the approximation of (44) is applied,

$$\Lambda_1^{\nu+1} = \Lambda_1^\nu - \frac{\tau}{2\eta^*} \sum_{m=1}^{M+1} h_m^\nu \left(P_{m-1}^{\nu+1} + P_m^{\nu+1} \right), \quad \Lambda_1^0 = 0. \quad (64)$$

Two definitions on the space nodal points will be used in computations:

$$x_m^\nu = \Lambda_1^\nu + \left(\frac{m}{M+1} \right)^s (\Lambda_2 - \Lambda_1^\nu), \quad m = 0, \dots, M+1, \quad (65)$$

for $s = 3/2$ or $s = 2$;

$$x_m^\nu = \Lambda_1^\nu + \frac{1 + \cos\left(\frac{2M+4-m}{2M+4}\pi\right)}{1 + \cos\left(\frac{M+3}{2M+4}\pi\right)} (\Lambda_2 - \Lambda_1^\nu), \quad m = 0, \dots, M+1. \quad (66)$$

Eq. (65) describes the power and Eq. (66), the Czebyshev–Gauss–Lobatto grids.

We define two linear implicit difference schemes: for the ordinary equation on pressure P and for the parabolic equation on concentration y_1 in system (42) with the initial-boundary conditions (45)–(48). For each ν , they are algebraical systems of $M+1$ equations with $M+1$ unknowns of the form

$$\begin{cases} y_m^0 = Y(x_m), & m = 0, \dots, M + 1, \\ P_0^0 = P_L(0), \\ A_{m-1}^0 P_{m-1}^0 + A_m^0 P_m^0 + A_{m+1}^0 P_{m+1}^0 = G(y_m^0), & m = 1, \dots, M, \\ P_{M+1}^0 = P_M^0, \end{cases} \tag{67}$$

$$\begin{cases} C_0^{v+1} = Y_L(t^{v+1}), \\ C_{m-1}^{v+1} y_{m-1}^{v+1} + C_m^{v+1} y_m^{v+1} + C_{m+1}^{v+1} y_{m+1}^{v+1} = y_m^v, & m = 1, \dots, M, \\ C_{M+1}^{v+1} = C_M^{v+1}, \end{cases} \tag{68}$$

$$\begin{cases} P_m^{v+1} = P_L(t^{v+1}), \\ A_{m-1}^{v+1} P_{m-1}^{v+1} + A_m^{v+1} P_m^{v+1} + A_{m+1}^{v+1} P_{m+1}^{v+1} = G(y_m^{v+1}), & m = 1, \dots, M, \\ P_{M+1}^{v+1} = P_M^{v+1}, \end{cases} \tag{69}$$

where

$$A_{m-1}^0 = \frac{1}{\hbar_m^0} \left(\frac{S(y_m^0)}{h_m^0} - \frac{1}{4\hbar_m^0} (y_{m+1}^0 - y_{m-1}^0) \right),$$

$$A_m^0 = -\frac{S(y_m^0)}{\hbar_m^0} \left(\frac{1}{h_{m+1}^0} + \frac{1}{h_m^0} \right) + Q,$$

$$A_{m+1}^0 = \frac{1}{\hbar_m^0} \left(\frac{S(y_m^0)}{h_{m+1}^0} + \frac{1}{4\hbar_m^0} (y_{m+1}^0 - y_{m-1}^0) \right),$$

$$S(y_m^0) = \frac{\Omega_2 B_2}{\Omega_1 B_1 - \Omega_2 B_2} + y_m^0,$$

$$\begin{aligned} G(y_m^0) &= -RT \left(\frac{\theta_m^0}{\Omega_1 + (\Omega_2 - \Omega_1) y_m^0} \frac{1}{\hbar_m^0} \left(\frac{y_{m+1}^0 - y_m^0}{h_{m+1}^0} - \frac{y_m^0 - y_{m-1}^0}{h_m^0} \right) \right. \\ &\quad \left. + \left(\frac{\theta_{m+1}^0}{\Omega_1 + (\Omega_2 - \Omega_1) y_{m+1}^0} - \frac{\theta_{m-1}^0}{\Omega_1 + (\Omega_2 - \Omega_1) y_{m-1}^0} \right) \frac{y_{m+1}^0 - y_{m-1}^0}{4(\hbar_m^0)^2} \right) \\ &\approx RT \left(-\frac{\theta_m^0}{\Omega_1 + (\Omega_2 - \Omega_1) y_m^0} \frac{1}{\hbar_m^0} \left(\frac{y_{m+1}^0 - y_m^0}{h_{m+1}^0} - \frac{y_m^0 - y_{m-1}^0}{h_m^0} \right) \right) \\ &\quad + RT \left(\frac{(\Omega_2 - \Omega_1) \theta_m^0}{(\Omega_1 + (\Omega_2 - \Omega_1) y_m^0)^2} \left(\frac{y_{m+1}^0 - y_{m-1}^0}{2\hbar_m^0} \right)^2 \right), \end{aligned}$$

$$A_{m-1}^{\nu+1} = \frac{1}{\hbar_m^\nu} \left(\frac{S(y_m^{\nu+1})}{h_m^\nu} - \frac{1}{4\hbar_m^\nu} (y_{m+1}^{\nu+1} - y_{m-1}^{\nu+1}) \right),$$

$$A_m^{\nu+1} = -\frac{S(y_m^{\nu+1})}{\hbar_m^\nu} \left(\frac{1}{h_{m+1}^\nu} + \frac{1}{h_m^\nu} \right) + Q,$$

$$A_{m+1}^{\nu+1} = \frac{1}{\hbar_m^\nu} \left(\frac{S(y_m^{\nu+1})}{h_{m+1}^\nu} + \frac{1}{4\hbar_m^\nu} (y_{m+1}^{\nu+1} - y_{m-1}^{\nu+1}) \right),$$

$$S(y_m^{\nu+1}) = \frac{\Omega_2 B_2}{\Omega_1 B_1 - \Omega_2 B_2} + y_m^{\nu+1},$$

$$\begin{aligned} G(y_m^{\nu+1}) &= -RT \left(\frac{\theta_m^{\nu+1}}{\Omega_1 + (\Omega_2 - \Omega_1) y_m^{\nu+1}} \frac{1}{\hbar_m^\nu} \left(\frac{y_{m+1}^{\nu+1} - y_m^{\nu+1}}{h_{m+1}^\nu} - \frac{y_m^{\nu+1} - y_{m-1}^{\nu+1}}{h_m^\nu} \right) \right. \\ &\quad \left. + \left(\frac{\theta_{m+1}^{\nu+1}}{\Omega_1 + (\Omega_2 - \Omega_1) y_{m+1}^{\nu+1}} - \frac{\theta_{m-1}^{\nu+1}}{\Omega_1 + (\Omega_2 - \Omega_1) y_{m-1}^{\nu+1}} \right) \frac{y_{m+1}^{\nu+1} - y_{m-1}^{\nu+1}}{4(\hbar_m^\nu)^2} \right) \\ &\approx RT \left(-\frac{\theta_m^{\nu+1}}{\Omega_1 + (\Omega_2 - \Omega_1) y_m^{\nu+1}} \frac{1}{\hbar_m^\nu} \left(\frac{y_{m+1}^{\nu+1} - y_m^{\nu+1}}{h_{m+1}^\nu} - \frac{y_m^{\nu+1} - y_{m-1}^{\nu+1}}{h_m^\nu} \right) \right) \\ &\quad + RT \left(\frac{(\Omega_2 - \Omega_1) \theta_m^{\nu+1}}{(\Omega_1 + (\omega_2 - \Omega_1) y_m^{\nu+1})^2} \left(\frac{y_{m+1}^{\nu+1} - y_{m-1}^{\nu+1}}{2\hbar_m^\nu} \right)^2 \right), \end{aligned}$$

$$C_{m-1}^{\nu+1} = \frac{B_1 \tau}{2\hbar_m^\nu h_m^\nu} ((w_m^\nu + \Omega_1) (P_m^\nu - P_{m-1}^\nu)) + \frac{\tau}{2\eta^* \hbar_m^\nu} \sum_{j=m+1}^{M+1} \frac{h_j^\nu}{2} (P_{j-1}^\nu + P_j^\nu),$$

$$C_m^{\nu+1} = 1 + \frac{\tau}{\eta^*} P_m^\nu - \frac{B_1 \tau}{\hbar_m^\nu} \left(\left(\frac{w_{m+1}^\nu}{h_{m+1}^\nu} - \frac{w_m^\nu}{h_m^\nu} \right) + \Omega_1 \left(\frac{P_{m+1}^\nu - P_m^\nu}{h_{m+1}^\nu} - \frac{P_m^\nu - P_{m-1}^\nu}{h_m^\nu} \right) \right),$$

$$C_{m+1}^{\nu+1} = -\frac{B_1 \tau}{2\hbar_m^\nu h_{m+1}^\nu} (w_{m+1}^\nu + \Omega_1) (P_{m+1}^\nu - P_m^\nu) - \frac{\tau}{2\eta^* \hbar_m^\nu} \sum_{j=m+1}^{M+1} \frac{h_j^\nu}{2} (P_{j-1}^\nu + P_j^\nu),$$

$$w_m^\nu = \frac{1}{2} (q_m^\nu + q_{m-1}^\nu) (y_m^\nu - y_{m-1}^\nu),$$

$$q_m^\nu = \frac{\Omega_1 (RT \Omega_2 y_m^\nu - \Omega_1 (y_m^\nu - 1) (RT + \Omega_2 E_{u_0}^{\mu_1}))}{y_m^\nu (\Omega_1 + (\Omega_2 - \Omega_1) y_m^\nu)^2},$$

for $\nu \in \mathbb{N} \cup \{0\}$.

If we consider a finite difference method for system (42) with the initial-boundary conditions (45)–(47), (53), then a discretization of (53) is as follows:

$$y_0^{v+1} = \frac{k_f \Omega_2 F - k_b}{B_1 \left(\frac{w_1^v}{h_1^v} + \Omega_1 \frac{P_1^v - P_0^v}{h_1^v} \right) + \frac{1}{2\eta^*} \sum_{i=1}^{M+1} (P_{i-1}^v + P_i^v) h_i^v - k_b}. \quad (70)$$